DR21 MAIN: A COLLAPSING CLOUD*

LARRY KIRBY
Department of Astronomy and Astrophysics, Enrico Fermi Institute, The University of Chicago, Chicago, IL 60637, USA; lkirby@oddjob.uchicago.edu

ABSTRACT

The molecular cloud, DR21 Main, is an example of a large-scale gravitational collapse about an axis near the plane of the sky where the collapse is free of major disturbances due to rotation or other effects. Using flux maps, polarimetric maps, and measurements of the field inclination by comparing the line widths of ion and neutral species, we estimate the temperature, mass, magnetic field, and the turbulent kinetic, mean magnetic, and gravitational potential energies, and present a three-dimensional model of the cloud and magnetic field.

Key words: ISM: magnetic fields – stars: formation – submillimeter – techniques: polarimetric

Online-only material: color figure

1. INTRODUCTION

Partially ionized material in a molecular cloud will respond to gravitational forces by moving, primarily, along magnetic field lines. If one assumes that the field is not significantly tangled by turbulence, one can expect a concentration of material in an oblate core. This model has been verified by the analysis of polarimetric and photometric data (J. L. Dotson et al. 2009, in preparation) by Tassis et al. (2009) showing that the field is directed along the short axes of the cores. The neutral component of the material will move slowly across field lines toward the center of gravity thus increasing the gravitational field. Where a pinch in the field is indicated by a polarization map, one can infer that the gravitational field in the core is competing with the support provided by the field. Within a critical radius, one expects the cloud to collapse.

Examples of pinched fields have been found in Orion (Schleuning 1998) and in NGC1333 (Girart et al. 2006). In the case of DR21 Main (DR21M), the polarization map extends to radii such that the field straightens out as the gravitational field diminishes leaving an hour glass field configuration. In this cloud, one has an opportunity to estimate the mass within the collapsing region. We use 350 μm polarimetry to measure the field as projected on the sky (Section 3.1); line-width measurements to estimate the inclination of the field to the line of sight (Section 4.1); photometric maps to estimate the mass distribution (Section 4.3); and the angular dispersion of the field vectors to estimate the field strength (Section 4.4).

2. DR21

The giant star-forming complex, DR21 (Figure 1) is located in the Cygnus constellation ∼3 kpc from Earth (Campbell et al. 1982). The southernmost component, DR21M, has a mass of ∼ 20,000 $M_\odot$ (Richardson et al. 1989). It contains one of the most energetic star formation outflows detected (Garden et al. 1991; Garden & Carlstrom 1992). Garden et al. (1991) measured the mass of the outflow to be 3000 $M_\odot$. Observers using *Spitzer* found five near-infrared (NIR) sources (see Figure 2) inside DR21M, presumed to be protostars (Kumar et al. 2007; Davis et al. 2007) indicating that regions within the

cloud are undergoing gravitational collapse. Glenn et al. (1999) at 1.3 mm and Minchin & Murray (1994) at 800 μm have previously measured the polarization of DR21 finding uniform position angles ∼ 25° east of north (i.e., *B* field ≈ 65° west of north). The galactic plane is oriented at 42° east of north. Roberts et al. (1997) measured a line-of-sight magnetic field of ∼400 μG using H I Zeeman measurements around the dust-emission peak and star formation regions. The regions observed by Roberts et al. (1997) with 3.5σ detections are outlined in green in Figure 3.

3. OBSERVATIONS

3.1. Polarization

Observations, made at the Caltech Submillimeter Observatory (CSO) with the polarimeter Hertz (Schleuning et al. 1997; Dowell et al. 1998), provided 350 μm polarization maps of the region. Hertz was later replaced by SHARP (Li et al. 2008), a module mounted ahead of the photometer SHARC-II (Dowell et al. 2003) to permit polarization measurements.

SHARP has a wire cross grid to split the incoming signal into orthogonal components of polarization which are then detected on two 144 pixel subsets of the SHARC-II detector array. Standard infrared techniques of chopping the secondary mirror to remove sky emission and positional offsets to remove gradients in sky emission were used for all the polarimetry observations (Hildebrand et al. 2000). The chopping direction was azimuthal with a throw of 300″. To avoid chopping into the adjacent cloud, DR21OH, all observations were made when the chop throw was > 30° from north–south on the sky. A half-wave plate was rotated to four different angles separated by 22°.5. Each observation cycle consisted of a set of observations at the four half-wave plate angles. The signals from the two 144 pixel arrays were then combined to give the polarization and photometric signals as described by Kirby et al. (2005). The polarization and flux signals are given by

$$\text{Polarization Signal} = H - V \qquad (1)$$

$$\text{Flux Signal} = H + V, \qquad (2)$$

where H and V are the horizontal and vertical components of the signal. The Stokes parameter, Q, was calculated from the difference of the polarization signals of the 1st and 3rd

---
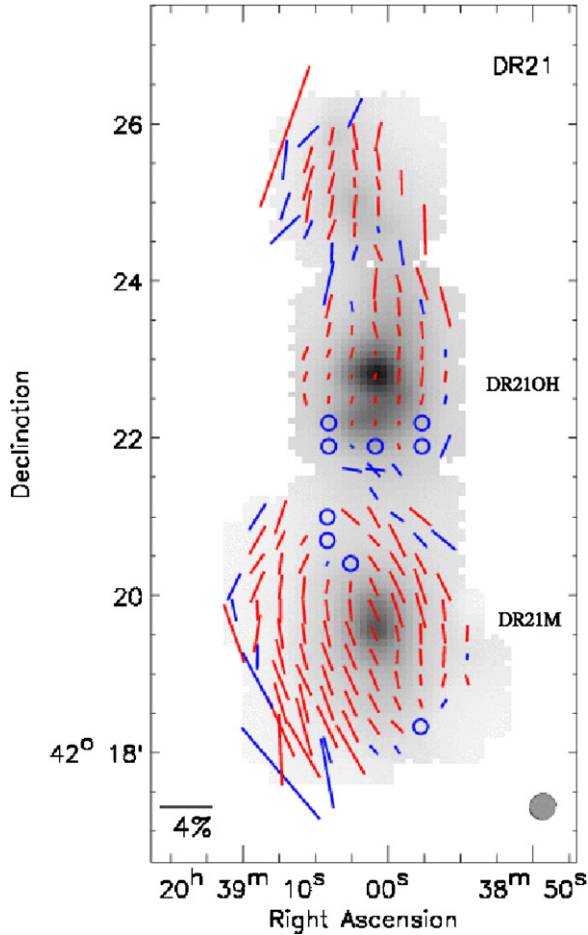
Figure 1. Hertz image (J. L. Dotson et al. 2009, in preparation) of the star-forming region DR21. Red vectors (E-vectors) are for measurements better than 3σ polarization and blue vectors are for measurements of $2\sigma–3\sigma$. Open circles are locations with a 2σ upper limit of 1%.

angles in the cycle, while the parameter U was calculated from the difference of the polarization signals of the 2nd and 4th angles. The source flux, I, was determined by the average of the flux signals from the four half-wave plate positions. The Q, U, and I from each cycle were then combined after correcting for changes in attenuation and sky noise. Due to the lack of an instrument rotator, this combination had to be done a new way. The corrected Q, U, and I from all of the cycles were combined to form an irregularly sampled map. This map was then smoothed to a resolution of $\sim 10''$ (for more detail see Houde & Vaillancourt (2007).

The observations were made in seven fields spaced by $45''$. Each field was observed with a four-point dither on corners of a square $10''$ wide in Right Ascension (R.A.) and Declination (decl.). A few additional observations were taken to fill in areas of low signal to noise in the above seven fields. The data were corrected for instrument polarizations of $\sim 0.3\%–0.5\%$ (Li et al. 2008; J. E. Vaillancourt et al. 2009, in preparation)

The SHARP observations were taken on 2006 July 15–19 during intermediate weather ($\tau_{225\ GHz} \approx 0.07–0.08$ corresponding to 1.7–2.0 mm zenith water vapor). The SHARP polarization data set shows 1270 sky positions with a signal to noise $\geqslant 3$. The beam size of SHARP is $\sim 4\times$ the pixel size. Limiting the sample so there is no beam overlap leaves 78 measurements. The median value of the polarization is 2.4% ranging between 0.37% and 13%. Half of the points have a signal to noise better

than 4.7. At this value, the accuracy of the position angle of the polarization vectors is $\sim 6°.5$. The direction of polarization shows a pinched or hourglass shape (see Figure 3). The axis of symmetry of the hourglass is inclined $\sim 15°$ east of north (determined by model, see Section 4.5.) The results tabulated by J. L. Dotson et al. (2009, in preparation) were obtained with the polarimeter, Hertz (Figure 3, blue dotted vectors). The Hertz measurements were taken on three observing runs, 1997 April 18–27, 1997 September 18–26, and 2001 April 10–16.

3.2. Heterodyne Measurements

The polarimetry measurements from SHARP and Hertz are supplemented with 345 GHz heterodyne measurements of ion and neutral molecular line widths from the CSO. The heterodyne measurements were taken on 2006 July 12–13 ($\tau_{225\ GHz} \approx 0.1$). The inclination of the field at eleven points within the pinched region was determined from measurements of line widths of neutral and ionized molecules of comparable mass. The heterodyne measurements of the $J \to 4$–3 transition in HCN and HCO+ were made using only on/off position differencing (Houde et al. 2000a, 2000b). The data were reduced using the CLASS program as part of the GILDAS package of programs (http://www.iram.fr/IRAMFR/GILDAS). Each of the lines was smoothed to half of the natural resolution using the CLASS routine SMOOTH to improve the signal to noise. One of the positions was removed due to low signal to noise. Another position was unusable because the bandwidth of the instrument was insufficient to image the entire line.

The spectrum at each position was then fitted by a multi-Gaussian model (Figure 4) to determine the line widths (more properly the standard deviation σ_v). Multiple Gaussians were used to account for the self-absorption seen in most of the positions, and for one-sided outflows, which can cause an artificial reduction in line widths if not accounted for properly. The effects from broad outflows were removed from two locations. The fits were done using the XGaussfit program from the FUSE package of software for IDL (http://fuse.pha.jhu.edu/analysis/fuse_idl_tools.html). Results of the fits are given in Table 1.

4. RESULTS

4.1. Inclination Angle

Houde et al. (2000a, 2000b) investigated the effect of a magnetic field on the velocities and ions in a partially ionized flow (not necessarily an outflow or jet but any situation where local mean velocity is not zero). For a significantly strong field, the ions were forced into gyromagnetic rotation about the magnetic field instead of following the flow. This rotation led to a reduction in line width and suppression of high-velocity wings. The line widths were derived for both the neutrals and ions. The ratio of the line widths depends only on the orientation of the neutral flow(s) and the inclination angle of the magnetic field with the line of sight (Houde et al. 2002, 2004). Assuming that the neutral component of the material is H_2 (mean molecular mass of 2.3), the square of the ratio of the ion to neutral line width is given in terms of the angle with the line of sight, α, by

$$\frac{\sigma_{l,i}^2}{\sigma_{l,n}^2} \approx \frac{e \cos\alpha^2 + f(0.16\cos\alpha^2 + 0.84\sin\alpha^2/2)(m_i/\mu_i - 1)^{-1}}{e \cos\alpha^2 + f\sin\alpha^2/2}$$
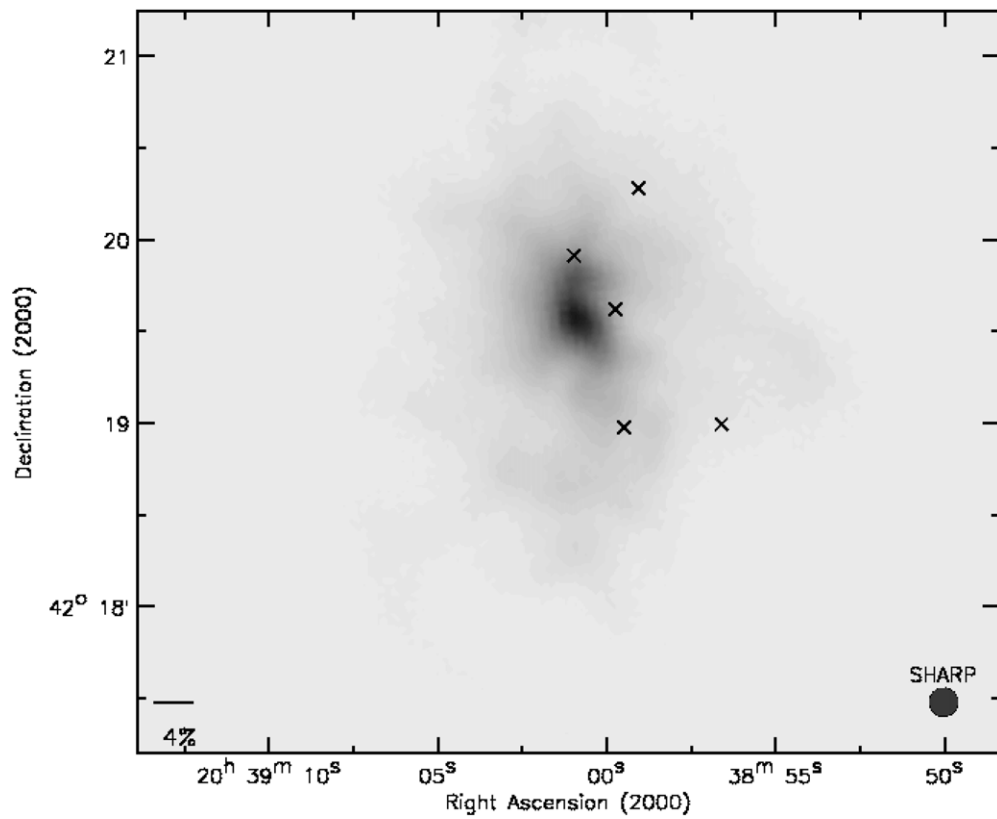
(3)

Figure 2. SHARC-II 350 μm flux map with ×s marking locations of *Spitzer* NIR sources (Kumar et al. 2007; Davis et al. 2007).

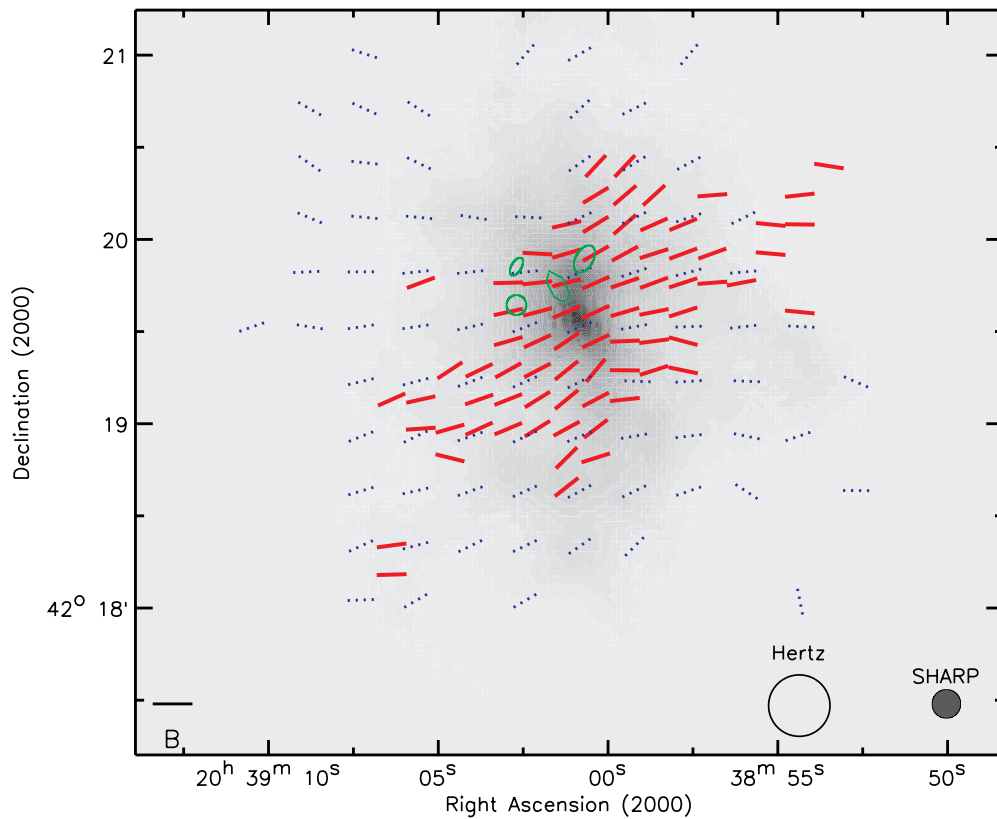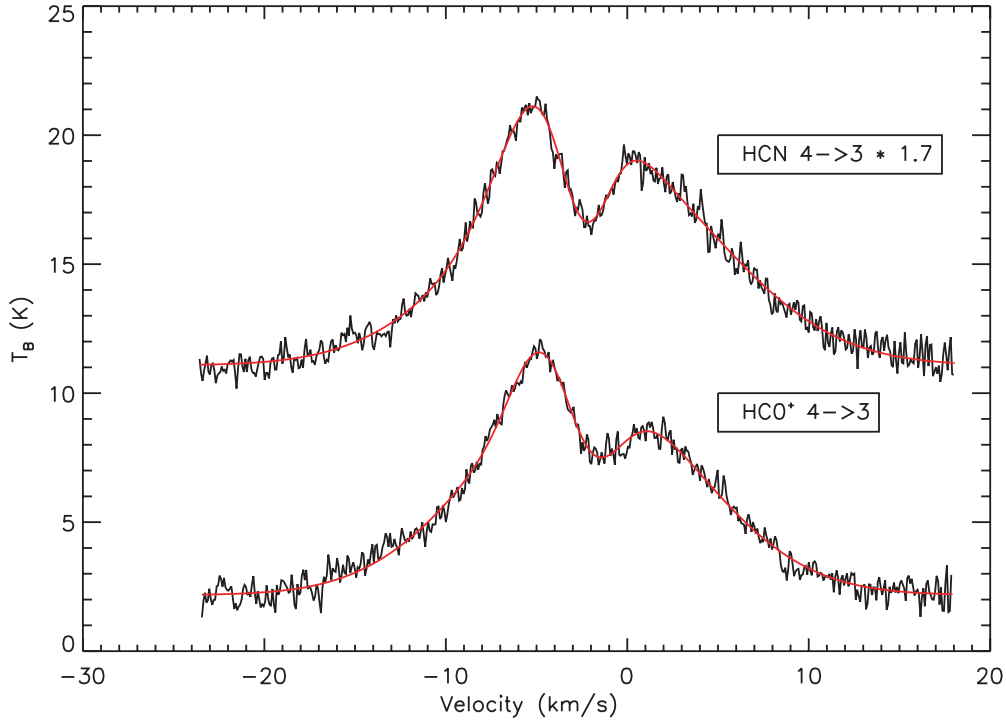**Figure 3.** 350 μm SHARP (red) and Hertz (blue dotted) polarization of DR21M. B vectors are all set to the same arbitrary length in the magnetic field direction. The gray-scale background comes from a SHARC-II flux map. Green contours show the locations larger than a SHARC-II pixel with 3.5σ Zeeman results from Roberts et al. (1997).

Figure 4. Line profile (black) and best-fit multi-Gaussian model (red) of the $J \rightarrow 4$–3 transition of HCN (top) and $J \rightarrow 4$–3 transition of HCO^{+} (bottom) at the center of DR21M ($20^{\mathrm{h}}37^{\mathrm{m}}14\overset{\mathrm{s}}{.}1$, $42°8'53''$).

Table 1
Line Width Data and Inclination Angle with the Line of Sight for DR21

ΔR.A.[a]	Δdecl.[a]	HCN σ_v (km s^{-1})	HCO^{+} σ_v (km s^{-1})	P (Hertz 350 μm)	α (deg)
0	0	6.4	6.2	1.2	39.3
20	0	4.9	4.8	1.95	28.3
−20	0	5.8	5.7	1.24	48.7
0	−20	4.8	4.4	1.36	45.2
0	20	3.5	3.2	1.84	43.5
−20	−20	5.4	4.3	1.09	61.6
−20	20	2.0	1.6	2.72	62.4
20	20	2.4	1.7	1.74	68.4
20	−40	2.5	1.3	2.46	77.1

Note. [a] Position offsets in arcseconds from $20^{\mathrm{h}}37^{\mathrm{m}}14\overset{\mathrm{s}}{.}1$, $42°8'53''$ (2000).

where

$$e = \frac{1 - \cos^3 \Delta\theta}{6}, \qquad (4)$$

$$f = \frac{2 - 3\cos\Delta\theta + \cos^3\Delta\theta}{6}, \qquad (5)$$

and m_i and μ_i are the ion mass and the reduced mass, respectively. The neutral flows are modeled as symmetrical and contained within a cone of width $\Delta\theta$ centered on magnetic field direction (symmetry axis, see Figure 5). All values of α must satisfy the condition $P/P_{\mathrm{max}} \leqslant \sin\alpha^2$ where P_{max} is the maximum polarization seen by Hertz (10%; Houde et al. 2004).

Although the cone half width, $\Delta\theta$, can, in principle, be determined by finding the curve that best fits the above condition on P/P_{max}, the data for DR21 do not provide significant constraints on this quantity. The values of α presented in Table 1 are computed assuming $\Delta\theta = 45°$. The inclination with the line of sight decreases toward the center of DR21 as would be expected for a magnetic field in the center of a gravitationally contracting region with an axis near the plane of the sky. Inclination angles for points located at the edge of the cloud, where the gravitational pinch has had only a small effect, should approximate the inclination of the cloud's mean B field. These points for DR21 give an estimate of $\sim 70°$ inclined to the line of sight or $\sim 20°$ to the plane of the sky.

Choosing the wrong value of $\Delta\theta$ leads to a systematic error in the calculation of each angle, but the difference between angles is not significantly affected. The overall trend of decreasing angle toward the center of the cloud remains. If, instead, we had assumed $\Delta\theta = 90°$, the values shown in the table would decrease by $\sim 15°$ but the overall trend toward decreasing inclinations toward the center would not change.

4.2. Temperature and Optical Depth

The spectral energy distribution (SED) at 350 and 850 μm was fitted to give estimates of the dust temperature and optical depth at 350 μm. The 850 μm map was acquired from the SCUBA online archive[1] (Project ID: m02bu47). The SHARC-II map at 350 μm was smoothed and repixelated to

---

[1] http://www2.cadc-ccda.hia-iha.nrc-cnrc.gc.ca/jcmt
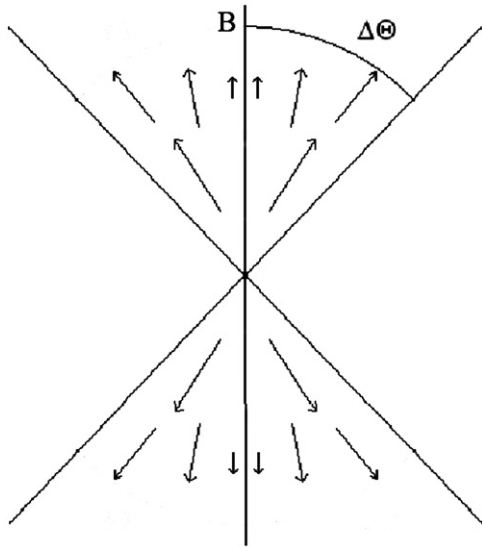
Figure 5. Illustration of flow of neutral material. All flows (velocity vectors) are contained within a cone of width $\Delta\theta$ centered on the symmetry axis defined by the magnetic field (see Figure 2 of Houde et al. 2002). Length of vectors is arbitrary as magnitude and direction are assumed independent.

match the 850 μm map. The intensity at frequency ν and corresponding wavelength λ was then modeled as

$$I_\nu = B_\nu(T)\left(1 - e^{-\tau_{350}(350/\lambda)^2}\right), \tag{6}$$

where the exponent gives the atmospheric transmission at frequency ν as determined from the transmission at 350 μm, and $B_\nu(T)$ is the Planck function at frequency ν and temperature T. An example fit to the data for the center of DR21 is shown in Figure 7. This formula assumes the cloud is optically thin at the wavelengths used. The ratio of the 350 μm flux to the 850 μm is constant throughout the majority of the cloud (~ 15) with a discrete jump at the edges of the cloud (~ 25) and a dip in the center (~ 8). The constancy of the ratio implies optical thinness except at the center where the ratio drops.

Temperatures at the peak were ~ 20 K and went up to ~ 25 K in the cloud. The edges of the cloud where the ratio increased had higher temperature (30–50 K). The 25 K region of the cloud extended along a rough northeast–southwest direction similar to the direction of the outflow. The optical depth showed a similar trend with a value at the peak greater than 1. The optical depth quickly drops below 1 indicating that all but the bright peak areas of DR21 main are optically thin at 350 μm, as expected from the flux ratios. Harvey et al. (1986) found temperatures from 50 μm and 100 μm flux maps to be ~ 50 K. These wavelengths may be coming from a different environment with a different temperature. Supporting a multienvironment hypothesis, Richardson et al. (1989) found a 350 μm to 800 μm ratio of ~ 16 at DR21OH with a corresponding temperature of ~ 25 K in regions given to be ~ 37 K by Harvey et al. (1986). Throughout the rest of the paper, we use temperatures of 20–25 K from the SHARP and SCUBA fluxes.

4.3. Mass

The mass of cloud within a specified region of a cloud can be determined from its temperature and far infrared flux (Hildebrand 1983)

$$M = \frac{FD^2}{B_\nu(T)}C_M, \tag{7}$$

where F is the flux, D is the distance to the cloud, and

$$C_M = [N(H + H_2)/\tau(\nu)]m_H\mu = 1.2 \cdot 10^{25}(350/400)^2 m_H\mu, \tag{8}$$

where $\tau(\nu)$ is the optical depth of the cloud at frequency ν. Within a radius of ~ 1 pc (size of SHARP map in the E-W direction), DR21 main has a mass of $\sim 25,000\ M_\odot$, comparing nicely to the $\sim 20,000\ M_\odot$ found by Richardson et al. (1989).

4.4. Magnetic Field Strength

Chandrasekhar & Fermi (1953) described a method to estimate the magnetic field in the plane of the sky. This method related the dispersion of the direction of starlight polarization from a straight line to the strength of the magnetic field,

$$B_{\mathrm{planeofsky}} = \sqrt{\frac{4\pi\rho}{3}}\frac{\sigma_{\mathrm{obs}}(v)}{\sigma_\beta} \tag{9}$$

where ρ is the density of the gas, $\sigma_{\mathrm{obs}}(v)$ is the observed line of sight velocity dispersion, and σ_β is the dispersion in polarization direction in the plane of the sky. The weaker the field, the greater the dispersion of the polarization vector.

The dispersion of the polarization vectors will be overestimated if it is taken with respect to the mean field. To determine the dispersion about the local magnetic field one must take into account the inclination of the mean field (Section 4.1) and the structure of the large-scale field due to nonturbulent effects such as gravitational collapse, expanding H II regions, and differential rotation (Hildebrand et al. 2009). A polarization map usually shows a smoothly-varying pattern of vectors; therefore at separations small compared to the cloud diameter, the two-point angular correlation function ($\sqrt{\langle\Delta\beta^2\rangle}$) of position angles should increase almost linearly as shown in the bottom panel of Figure 8. The linear portion would have a zero intercept if there were no measurement error and no turbulence. Both effects will cause the whole two-point correlation to be displaced upward (except at values < correlation length of turbulence which is expected to be much less than the SHARP or Hertz resolution of DR21). The y-intercept, b, of the best-fit line is then the quadratic sum of the estimate of the dispersion, σ_β, and the measurement error, $\sigma_m e$. A cross correlation of repeat observations gives the estimate of the measurement error (value at 0 separation) and an estimate of the quadratic sum of measurement error and turbulent dispersion (intercept of best-fit line to linear region at small nonzero separation)

$$b = \sqrt{\sigma_\beta^2 + \sigma_{\mathrm{me}}^2}. \tag{10}$$

Figure 8 shows the correlation function for two subsets of the Hertz data set. The subsets were constructed by taking every other raw data file starting with file 1 for subset 1 and file 2 for subset 2. The line best fit to the linear region of the correlation function has an intercept of $9°3$. The value of the correlation function at zero separation is $7°6$ giving an estimate of $5°3$ for the turbulent dispersion. Using the Chandrasekhar and Fermi method formula with correction factor from Ostriker et al. (2001) gives a plane of the sky magnetic field of 3.1 mG where $\sigma_{\mathrm{obs}}(v)$ is the observed line-of-sight velocity dispersion of HCN measured to be 4.2 km s^{-1} and ρ is the mean density calculated from the mass in Section 4.3 to be 4.4×10^{-19} g cm^{-3}.

The method of data acquisition of SHARP prevents repeat observations of the same location (caused by lack of instrument rotator) preventing that sample from being split as done for
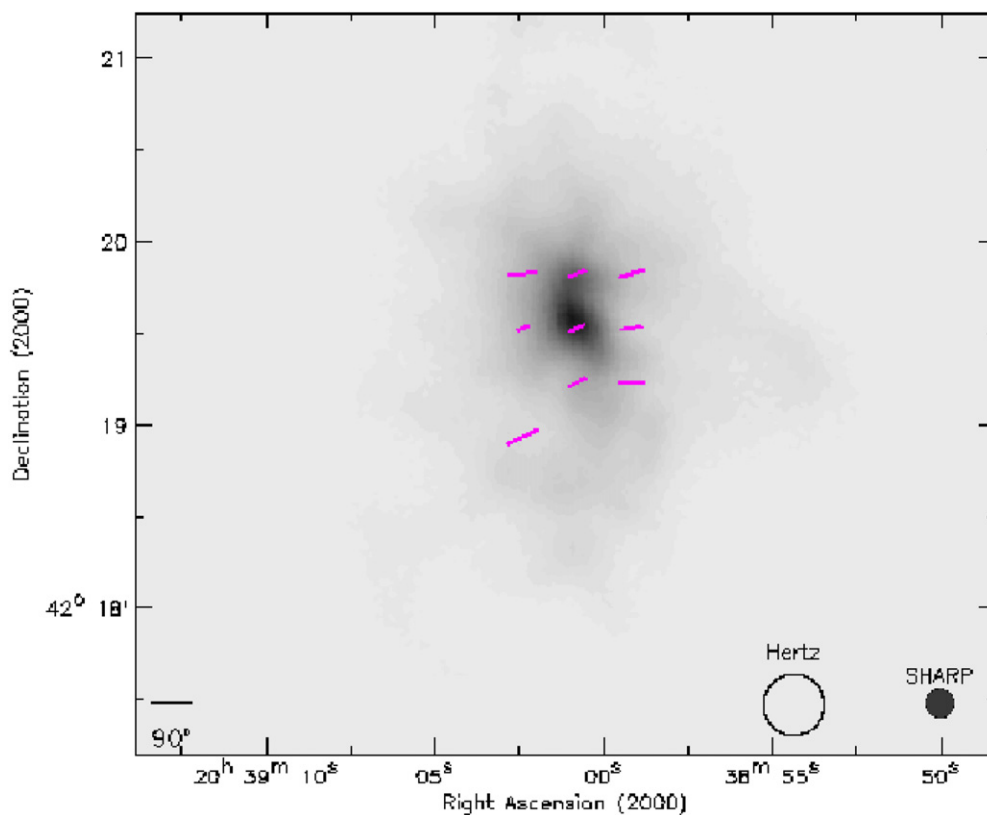
Figure 6. Polarization vectors with known three-dimensional spatial orientation. The angle of the vectors is drawn at the angle of the magnetic field in the plane of the sky. The length of the vector is proportional to the angle, α, of the magnetic field with respect to the line of sight. The gray-scale background is from SHARC-II.

(A color version of this figure is available in the online journal.)
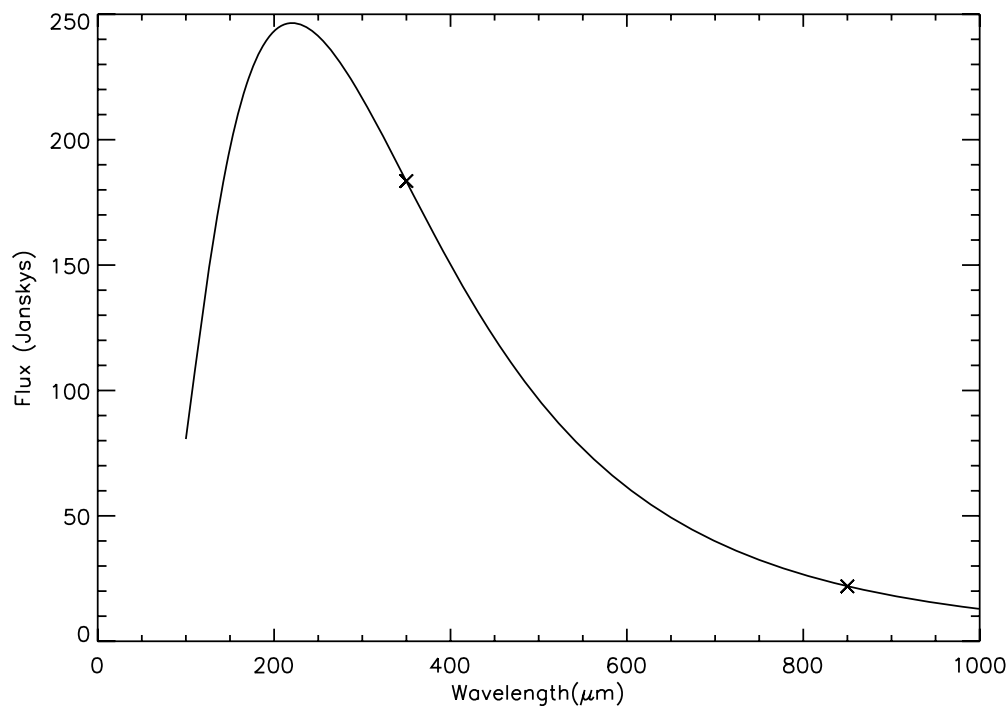
Figure 7. SED of the center region of DR21 with a fit from Equation (6). Cross symbols denote data points and the line is fitted from Equation (6).

Hertz. However, the mean of the individual errors on the angles gives a good estimate for the measurement error (7.°2 to 7.°6 for Hertz). Using that method of estimating the mean error and fitting a line to the linear region of the correlation function gives a magnetic field estimate of 2.5 mG using SHARP data (dispersion of 6.°6).
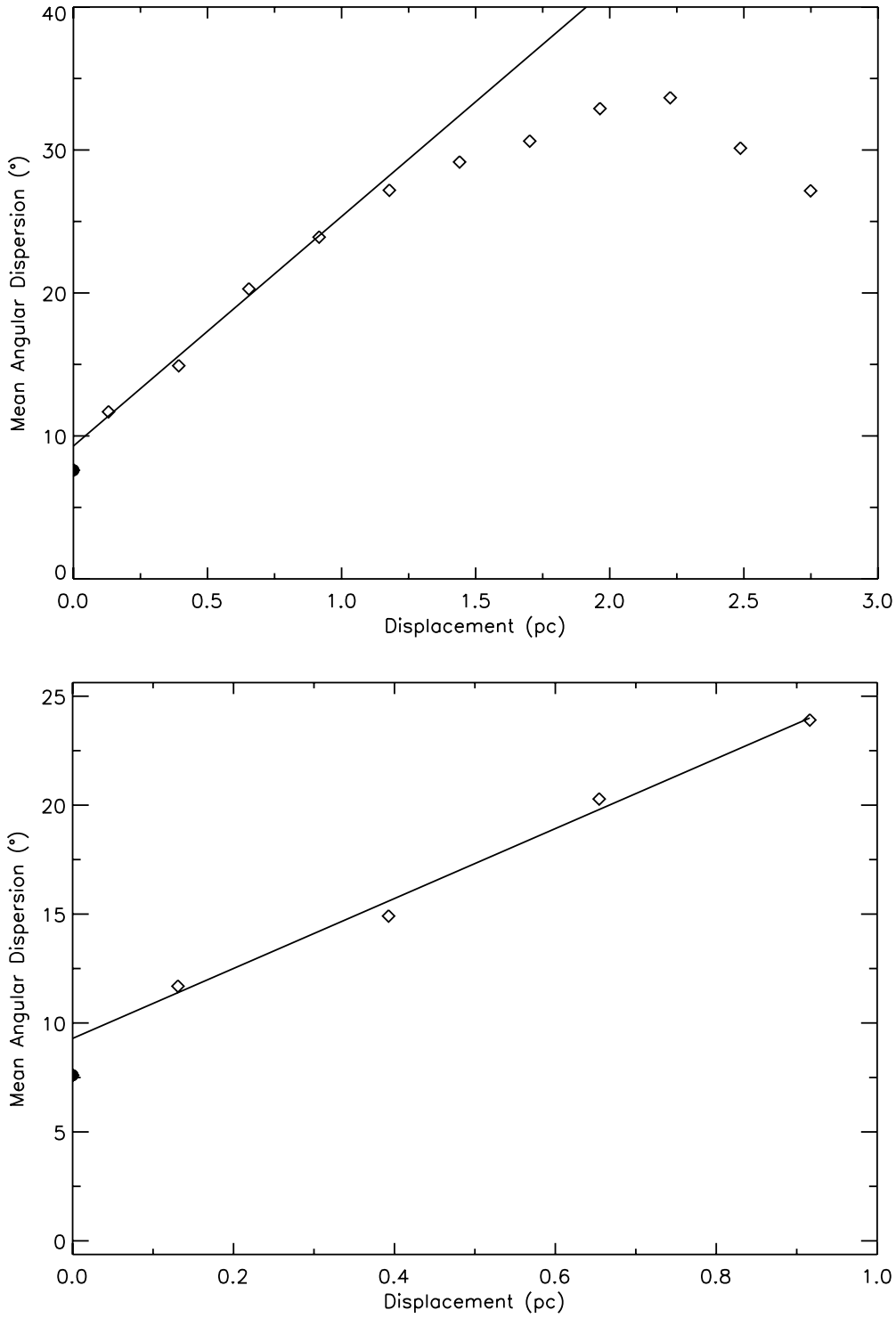
Figure 8. Two-point angular correlation function of the polarization angle of DR21 from two separate subsets of Hertz data. The top figure shows the whole cloud and the bottom figure shows the same function at separations $\leqslant\sim\frac{1}{4}$ of the major axis. The black circle shows value of the function at 0 separation.

Using the measurement of 400 μG for the line-of-sight magnetic field by Roberts et al. (1997) and taking a ~ 3 mG field in the plane of the sky gives a total magnetic field of ~ 3 mG inclined to the plane of the sky at $\sim 10°$. This estimate of the angle is probably low due to the Zeeman measurement being from H I, which exists at lower density than the dust we observe

in polarization so the field strength is also likely lower there. Taking the scaling of Heiles & Crutcher (2005) and the density of the region observed in H I as $\geqslant 10^3$, the angle with respect to the plane of the sky is $\leqslant 53°$. For a density of 10^4 cm^{-3}, the angle would be $\sim 20°$. Roberts et al. (1997) assumed that the magnetic field was less than 1 mG because unless the field was
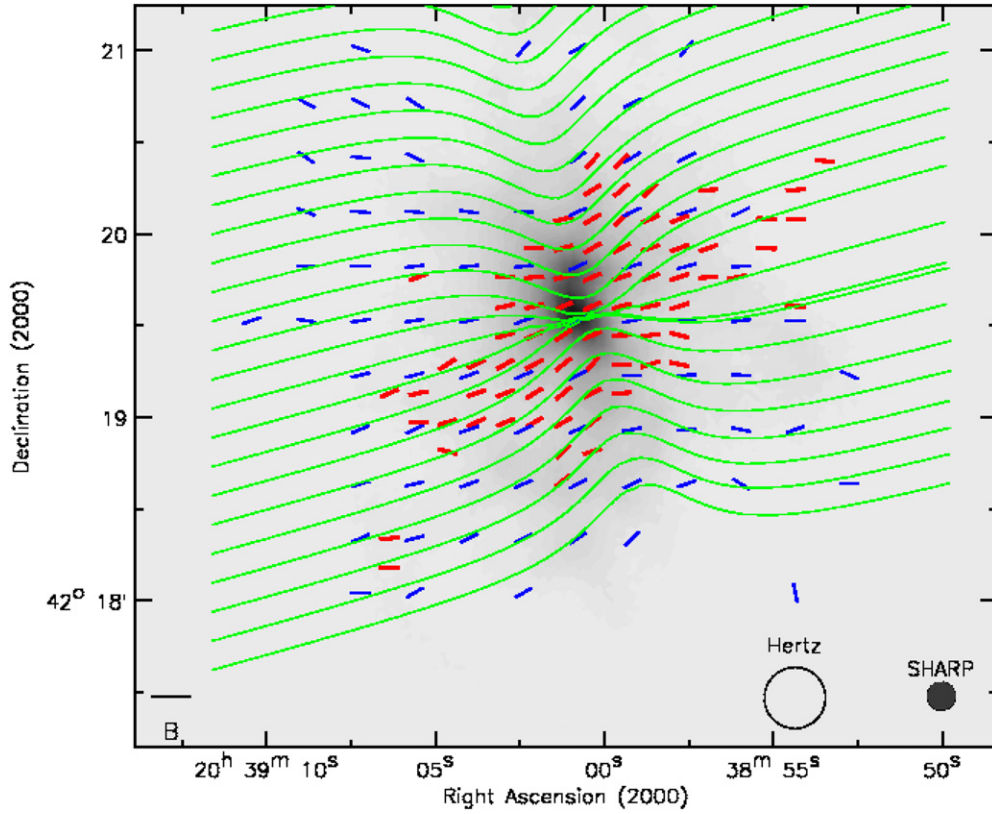
Figure 9. 350 μm SHARP polarization map (red vectors) with overplot of projected plane of sky vectors from three-dimensional fit.

very uniform, the field would have bent somewhere such that they detected a 1 mG field. The dust polarization measurements show a field that is very uniform implying the field could be larger than 1 mG and not detected in the Zeeman observations.

4.5. Three-Dimensional Model

A three-dimensional model of the flux and magnetic field was constructed and fitted to the observed flux and polarization data. The flux was modeled as a Gaussian ellipsis of the form

$$F \propto \exp\left[-\frac{x^2}{a^2} - \frac{y^2 + z^2}{b^2}\right], \qquad (11)$$

where x is the coordinate along the symmetry axis of the magnetic field, y and z are the other two Cartesian coordinates, and a and b are widths of the Gaussians to be fitted. The magnetic field was modeled as

$$B = \left(B_x, \frac{d}{dx}\left(\frac{cx^2}{x^2+d}\right)\frac{y}{\sqrt{y^2+z^2}}, \frac{d}{dx}\left(\frac{cx^2}{x^2+d}\right)\frac{z}{\sqrt{y^2+z^2}}\right), \qquad (12)$$

where

$$B_x \propto \int_{-\infty}^{\infty} F dx. \qquad (13)$$

This form was chosen to give a magnetic field with the shape of an hourglass that straightens at large distance from the center. The magnetic field strength in the x direction in the midplane was set proportional to the column density. Assuming flux freezing, the magnetic field strength in the x direction for locations outside the midplane was set to a value in the midplane that is found

by tracing the field line back to the midplane. The field in the $y - z$ plane was assumed radial and the strength was found from the strength in the x direction and the overall magnetic field direction. The flux and magnetic field strengths were then rotated and summed along the line of sight. The values of a, b, c, and d were then set to give the best fit to the flux and the magnetic field direction determined by the polarization measurements. The best-fit values were $a = 5, b = 15, c = 10, d = 90$ (units for a, b, c, d are SHARP pixels $= 2.''375$, $20°$ for the angle of the magnetic field with the plane of the sky, and $15°$ east of north for the angle of the projected minor axis on the plane of the sky). The fit for the magnetic field direction was quite good (chi-squared of ~ 2). The flux fit was poor as DR21-Main is not an exact ellipse. Figure 9 shows the model vectors along with the SHARP vectors. The angle with the plane of the sky is somewhat higher than that found in Section 4.4 but agrees well with the measured inclination angles farthest from the center (see Section 4.1).
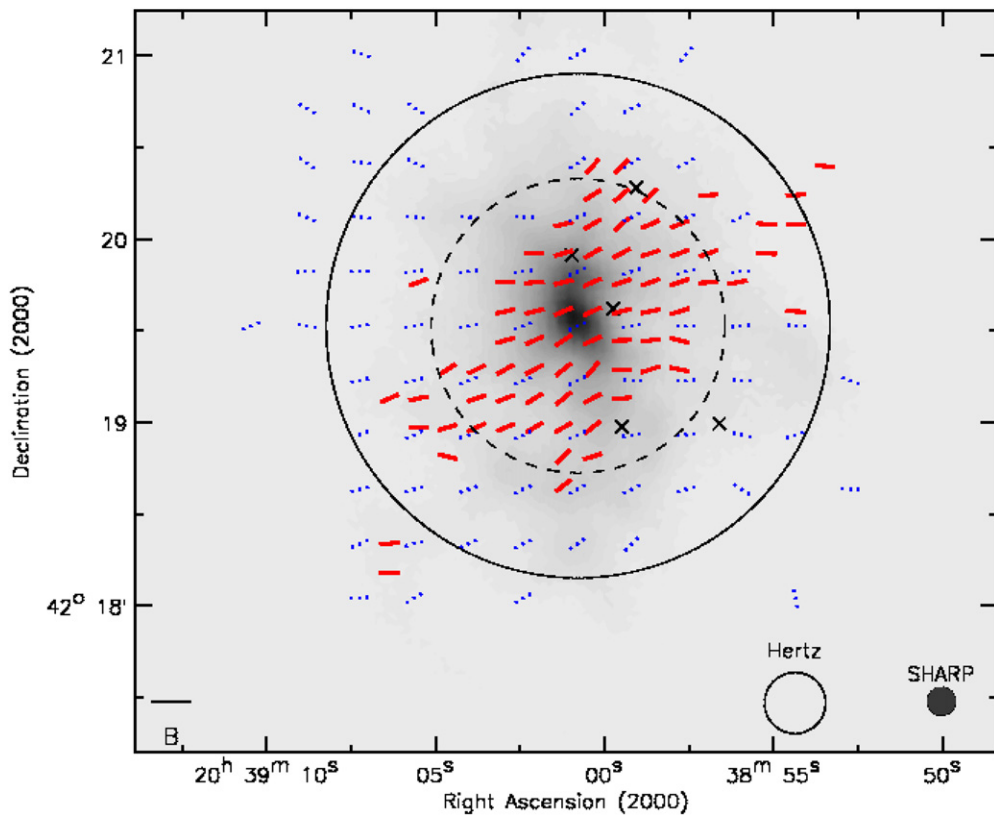
4.6. Gravitational and Magnetic Potential Energies

Using the mass and magnetic field estimates discussed in Sections 4.3, 4.4, and the three-dimensional model presented in Section 4.5, one can estimate the dependence on radius of the gravitational and magnetic potential energies. The gravitational potential energy of a flattened centrally condensed spheroid at a radius R centered on the peak of the cloud is

$$E_{grav} = \frac{3aGM^2}{5R}, \qquad (14)$$
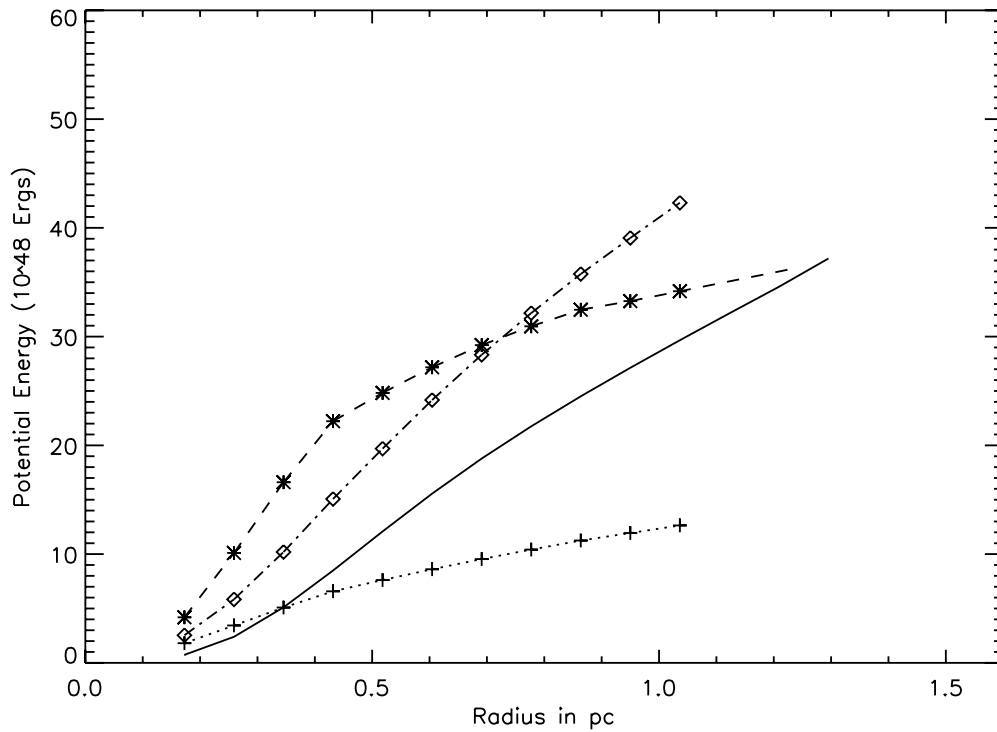
Figure 10. Gravitational potential (dashed line and asterisks) is computed from the calculation of mass (Section 4.3). The magnetic field energy (solid line) is based on determination of magnetic field strength using the two-dimensional CF method and published Zeeman measurements (Section 4.4) assuming equipartition between the uniform and fluctuating field (Novak et al. 2007). Recent results (Hildebrand et al. 2009) show that equipartition is an overestimate and that the ratio of the turbulent to mean field is approximately 10%. The turbulent energy (dotted line and crosses) is calculated from the mass and observed HCN line widths. The dot-dashed line and squares is the sum of magnetic and turbulent energies.

Figure 11. DR21M with SHARP magnetic field vectors. Solid circle delineates radius where magnetic energy becomes larger than gravitational potential energy. Dotted circle delineates radius where the sum of magnetic and turbulent energy becomes larger than gravitational potential energy assuming equipartition. The gray-scale background is from SHARC-II and black "x"s mark the location of *Spitzer* point objects.
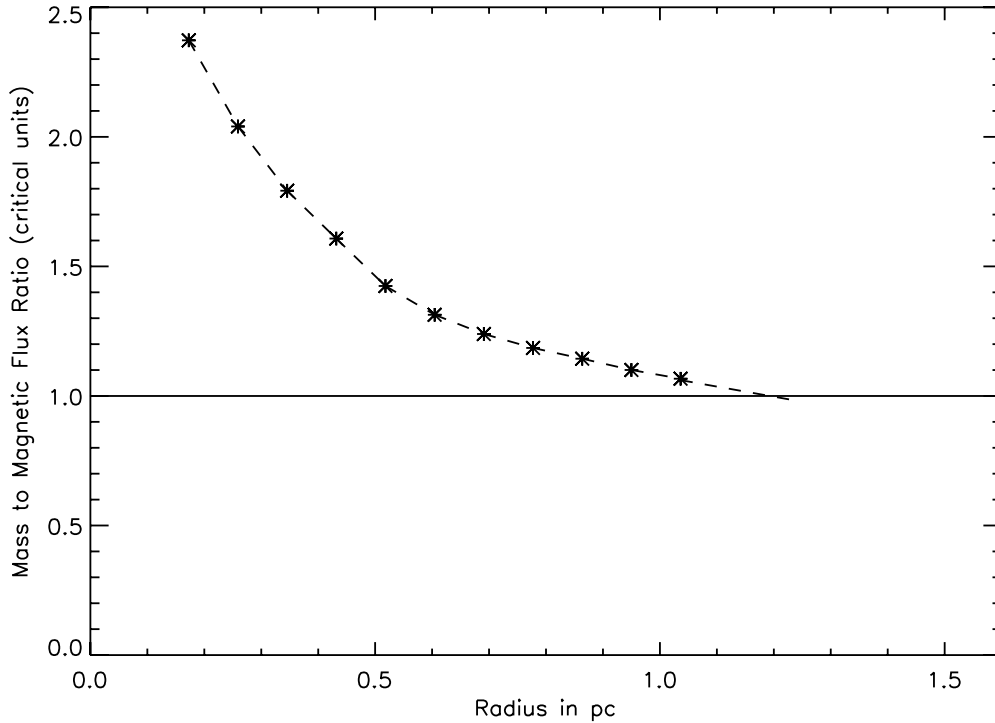
Figure 12. Mass to flux ratio in units of the critical ratio between supercritical and subcritical. Asterisks are calculations of the ratio and dashed line is the interpolation/extrapolation.

and the magnetic energy of the uniform field is given by

$$E_{\mathrm{mag}} = \frac{B^2 R^3 b}{6}, \qquad (15)$$

where the values $a = 1.2$ and $b = 0.3$ are calculated by setting the energies equal when the mass to magnetic flux ratio is the critical value (McKee et al. 1993). B is scaled according the model in Section 4.5 and normalized such that the energy inside 1 pc is the same as for the mean field calculated in Section 4.4. By comparing large-scale polarization maps with magnetohydrodynamic turbulence simulations, Novak et al. (2007) found that the ratios of the uniform to fluctuating magnetic field in the clouds NGC 6334 and G333.6-0.2 were in the range 0.6–2.0. Figure 10 shows the gravitational and magnetic potential energies (assuming a ratio between uniform to fluctuating field of 1) versus radius. Extrapolating the gravitational potential energy curve to find the radius at which the two energies are equal gives an estimate of ~ 1.2 pc. The dotted line in Figure 10 shows turbulent energy calculated from the average HCN line widths of 4.2 km s^{-1} and assuming the velocities are isotropic. The sum of these two energies is the dotted-dashed line that intersects the gravitational energy curve at 0.7 pc. One would then expect the critical radius to be between 0.7 and 1.2 pc. The critical radius should not be regarded as the radius which is supported against collapse since the virial theorem cannot be applied in this way to magnetic clouds (Mouschovias 1987, 1991; Dib et al. 2007). Figure 12 shows a plot of the mass to magnetic flux ratio versus radius. The ratio is in units of the critical value of the ratio defined by Mouschovias & Spitzer (1976)

$$M/\Phi_B = c_\Phi/\sqrt{G}, \qquad (16)$$

where c_Φ is taken to be 0.12 (Tomisaka et al. 1988). The ratio dips below the critical ratio at ~ 1.2 pc. The mass inside this

region is $\sim 25{,}000 M_\odot$ (Section 4.3) which is approximately the entire mass of the cloud. Figure 11 shows the polarization vectors with circles at the critical radii with and without turbulent energy. The magnetic field configuration changes at around these radii from the pinched structure to the east–west mean direction (see Figure 3). This geometry implies that the cloud is relatively stable against collapse at these radii, implying that the magnetic field is providing a significant amount of support against collapse. However the presence of protostars in radii greater than 1.2 pc in Figure 11 suggests that the true picture may be more complex.

5. SUMMARY

We present a three-dimensional model of the molecular cloud DR21 (Main). Polarimetry at 350 μm has provided a map of the magnetic field as projected on the plane of the sky; line observations of ion and neutral molecules have provided measurements of the inclination of the field to the line of sight; photometry has provided column densities and 350 μm/850 μm color temperatures.

A three-dimensional model of an hourglass configuration magnetic field inclined to the line of sight is fitted to the observations. We find a pinched field with an axis of $10°$–$20°$ from the plane of the sky. The mean-field strength is ~ 3 mG. The gravitational potential energy is equivalent to energies from support mechanisms (magnetic field and turbulence) at a radius between ~ 0.8 pc and 1.1 pc, a region encompassing $\sim 20{,}000\ M_\odot$.

REFERENCES

Campbell, M. F., Hoffmann, W. F., Thronson, H. A., Jr., Niles, D., Nawfel, R., & Hawrylycz, M. 1982, ApJ, 261, 550
Chandrasekhar, S., & Fermi, E. 1953, ApJ, 118, 113
Davis, C. J., Kumar, M. S. N., Sandell, G., Froebrich, D., Smith, M. D., & Currie, M. J. 2007, MNRAS, 374, 29
Dib, S., Kim, J., Vázquez-Semadeni, E., Burkert, A., & Shadmehri, M. 2007, ApJ, 661, 262
Dowell, C. D., et al. 2003, Proc. SPIE, 4855, 73
Dowell, C. D., Hildebrand, R. H., Schleuning, D. A., Vaillancourt, J. E., Dotson, J. L., Novak, G., Renbarger, T., & Houde, M. 1998, ApJ, 504, 588
Garden, R. P., & Carlstrom, J. E. 1992, ApJ, 392, 602
Garden, R., Hayashi, M., Gatley, I., Hasegawa, T., & Kaifu, N. 1991, ApJ, 374, 540
Girart, J. M., Rao, R., & Marrone, D. P. 2006, Science, 313, 812
Glenn, J., Walker, C. K., & Young, E. T. 1999, ApJ, 511, 812
Harvey, P. M., Joy, M., Lester, D. F., & Wilking, B. M. 1986, ApJ, 300, 737
Heiles, C., & Crutcher, R. 2005, in Cosmic Magnetic Fields, ed. R. Wielebinski & R. Beck (Berlin, Germany: Springer), 137
Hildebrand, R. H. 1983, QJRAS, 24, 267
Hildebrand, R. H., Davidson, J. A., Dotson, J. L., Dowell, C. D., Novak, G., & Vaillancourt, J. E. 2000, PASP, 112, 1215
Hildebrand, R. H., et al. 2009, ApJ, in press
Houde, M., Bastien, P., Peng, R., Phillips, T. G., & Yoshida, H. 2000a, ApJ, 536, 857
Houde, M., Dowell, C. D., Hildebrand, R. H., Dotson, J. L., Vaillancourt, J. E., Phillips, T. G., Peng, R., & Bastien, P. 2004, ApJ, 604, 717
Houde, M., Peng, R., Phillips, T. G., Bastien, P., & Yoshida, H. 2000b, ApJ, 537, 245
Houde, M., & Vaillancourt, J. E. 2007, PASP, 119, 871
Houde, M., et al. 2002, ApJ, 569, 803
Kirby, L., Davidson, J. A., Dotson, J. L., Dowell, C. D., & Hildebrand, R. H. 2005, PASP, 117, 991
Kumar, M. S. N., Davis, C. J., Grave, J. M. C., Ferreira, B., & Froebrich, D. 2007, MNRAS, 374, 54
Li, H., Dowell, C. D., Kirby, L., Novak, G., & Vaillancourt, J. E. 2008, Appl. Opt., 47, 422
McKee, C. F., Zweibel, E. G., Goodman, A. A., & Heiles, C. 1993, in Protostars and Planets III, ed. E. H. Levy & J. I. Lunine (Tucson, AZ: Univ. Arizona Press), 327
Minchin, N. R., & Murray, A. G. 1994, A&A, 286, 579
Mouschovias, T. C. 1987, in Physical Processes in Interstellar Clouds, ed. G. E. Morfill & M. Scholer (Dordrecth: Reidel), 453
Mouschovias, T. C. 1991, in The Physics of Star Formation and Early Stellar Evolution, ed. C. J. L. N. D. Kylafis (Dordrecht: Kluwer), 61
Mouschovias, T. C., & Spitzer, L., Jr. 1976, ApJ, 210, 326
Novak, G., Dotson, J. L., & Li, H. 2007, ApJ, submitted (arXiv:0707.2818)
Ostriker, E. C., Stone, J. M., & Gammie, C. F. 2001, ApJ, 546, 980
Richardson, K. J., Sandell, G., & Krisciunas, K. 1989, A&A, 224, 199
Roberts, D. A., Dickel, H. R., & Goss, W. M. 1997, ApJ, 476, 209
Schleuning, D. A. 1998, ApJ, 493
Schleuning, D. A., Dowell, C. D., Hildebrand, R. H., Platt, S. R., & Novak, G. 1997, PASP, 109, 307
Tassis, K., Dowell, C. D., Hildebrand, R. H., Kirby, L., & Vaillancourt, J. E. 2009, MNRAS, submitted
Tomisaka, K., Ikeuchi, S., & Nakamura, T. 1988, ApJ, 335, 239